Heliyon 10 (2024) e37955

Contents lists available at ScienceDirect

Heliyon

journal homepage: www.cell.com/heliyon

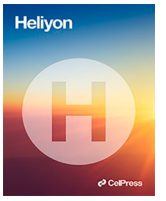

Research article

Prediction of high-risk prostate cancer based on the habitat features of biparametric magnetic resonance and the omics features of contrast-enhanced ultrasound

Fangyi Huang, Qun Huang, Xinhong Liao, Yong Gao *

Department of Ultrasound, First Affiliated Hospital of Guangxi Medical University, 6 Shuangyong Rd, Nanning, 530021, Guangxi, China

ARTICLE INFO

Keywords:
Habitat imaging
Omics features
Bp-MRI
CEUS
Prostate cancer

ABSTRACT

Rationale and objectives: To predict high-risk prostate cancer (PCa) by combining the habitat features of biparametric magnetic resonance imaging (bp-MRI) with the omics features of contrast-enhanced ultrasound (CEUS).

Materials and methods: This study retrospectively collected patients with PCa confirmed by histopathology from January 2020 to June 2023. All patients underwent bp-MRI and CEUS of the prostate, followed by a targeted and transrectal systematic prostate biopsy. The cases were divided into the intermediate-low-risk group (Gleason score $\leq$7, n = 59) and high-risk group (Gleason score $\geq$8, n = 33). Radiomics prediction models, namely, MRI_habitat, CEUS_intra, and MRI-CEUS models, were developed based on the habitat features of bp-MRI, the omics features of CEUS, and a merge of features of the two, respectively. Predicted probabilities, called radscores, were then obtained. Clinical-radiological indicators were screened to construct clinic models, which generated clinic scores. The omics–clinic model was constructed by combining the radscore of MRI-CEUS and the clinic score. The predictive performance of all the models was evaluated using the receiver operating characteristic curve.

Results: The area under the curve (AUC) values of the MRI-CEUS model were 0.875 and 0.842 in the training set and test set, respectively, which were higher than those of the MR_habitat (training set: 0.846, test set: 0.813), CEUS_intra (training set: 0.801, test set: 0.743), and clinic models (training set: 0.722, test set: 0.611). The omics–clinic model achieved a higher AUC (train set: 0.986, test set: 0.898).

Abbreviations: PI-RADS, prostate imaging reporting and data system; PCa, prostate cancer; csPCa, clinically significant prostate cancer; bp-MRI, biparametric magnetic resonance imaging; mpMRI, multiparameter MRI; T2WI, T2-weighted imaging; T2WI-FS, T2-weighted imaging fat saturation; DWI, diffusion-weighted imaging; ADC, apparent diffusion coefficient; CEUS, contrast-enhanced ultrasound; TRUS, transrectal ultrasound; ROI, region of interest; VOI, volume of interest; ICC, intraclass correlation coefficient; CH, Calinski-Harabasz; ROC, receiver operating characteristic; AUC, area under the curve; DCA, decision curve analysis; LASSO, least absolute shrinkage and selection operator; MLP, multilayer perceptron; LR, logistic regression; BMI, body mass index; T-PSA, total prostate-specific antigen; F-PSA, free prostate-specific antigen; PV, prostate volume; PSAD, PSA density; ALP, alkaline phosphatase; ALB, albumin; LYM, lymphocyte; NEU, neutrophil; MONO, mononuclear; NLR, neutrophil-to-lymphocyte count ratio; BM, bone metastasis; PI, peak intensity; TTP, time to peak; 95%CI, 95 % confidence interval; ACC, accuracy; SEN, sensibility; SPE, specificity; PPV, positive predictive value; NPV, negative predictive value; PRE, precision; FOV, field of view; NXE, number of excitations; TR, repetition time; TE, echo time; DICOM, Digital Imaging and Communications in Medicine.

* Corresponding author.
E-mail address: yonggaogx@163.com (Y. Gao).

https://doi.org/10.1016/j.heliyon.2024.e37955
Received 20 February 2024; Received in revised form 22 August 2024; Accepted 13 September 2024
Available online 16 September 2024

Conclusions: The combination of the habitat features of bp-MRI and the omics features of CEUS can help predict high-risk PCa.

1. Introduction

Prostate cancer (PCa) is the fifth highest cause of cancer death in men in 2020 [1]. In recent years, the incidence and mortality rates of PCa have increased significantly in China [2]. PCa with different risk degrees has different treatments and prognoses [3]. Currently, the gold standard for diagnosing PCa is ultrasound-guided prostate biopsy [4]. Recently, MRI-targeted biopsy, MRI-US fusion biopsy, and cognitive biopsy have been developed to optimize prostate biopsy [5]. MRI targeted biopsy is guided by a real-time scanning T2WI sequence. Although this technology can accurately locate the lesion, the process is too cumbersome and the equipment requirements are too high to popularize it in clinical practice [6]. An MRI-US cognitive biopsy is carried out by the operator through a visual comparison of pre-biopsy MRI images and real-time ultrasound images. Although this technology is easy to promote in clinical practice because of its simplicity and low equipment requirements, it is limited by the operator's knowledge and small suspect lesions [5,7]. MRI-US fusion biopsy is performed by software that superimposes suspicious lesions on the MRI onto real-time ultrasound images. Although this technique can reduce operator errors in visual registration by adjusting biopsy trajectories in real time through jointly displayed targets, there is a barrier presented by the cost of software [8]. Studies have shown that there is no significant difference in the detection rate of clinically significant PCa among the above three technologies [9]. However, biopsy only obtains a small portion of the tumor, which may ignore the heterogeneity of the tumor [10]. Therefore, a non-invasive method that can accurately describe the heterogeneity of tumors and predict the risk of PCa will have high clinical application value for patients.

MRI is considered an indispensable imaging technique for diagnosing PCa. Currently, studies have found that biparametric MRI (bp-MRI) has comparable diagnostic efficacy of clinically significant PCa to multiparameter MRI (mpMRI) [11,12]. Contrast-enhanced ultrasound (CEUS) can display real-time dynamic perfusion of the prostate and provide information about the tumor blood supply [13]. However, current imaging methods in clinical practice find it difficult to evaluate heterogeneity within prostate tumors [14,15].

Radiomics can effectively characterize subtle changes in images that are not observable by the naked eye [16]. The combination of radiomics features and advanced machine learning algorithms can quantitatively analyze the pathophysiological status of tumors, greatly improving the efficiency and accuracy of clinical diagnosis [17]. However, radiomics which still analyzes the entire tumor region, may ignore phenotypic variations in different regions, and may have bias in quantifying heterogeneity within the tumor [18]. To more effectively characterize intratumoral heterogeneity, habitat analysis was developed. This method generates different habitat subregions clustered according to the similarity of voxel-imaging features in the image, with the same subregion sharing common tumor biological pattern characteristics [19]. At the microscopic level, these subregions correspond to clusters of cells with similar genotypes and biological phenotypes, which can reflect the distribution of tumor cells and their molecular properties and better quantify intratumoral heterogeneity [20,21]. At present, few studies have combined the radiomics characteristics of MRI habitat

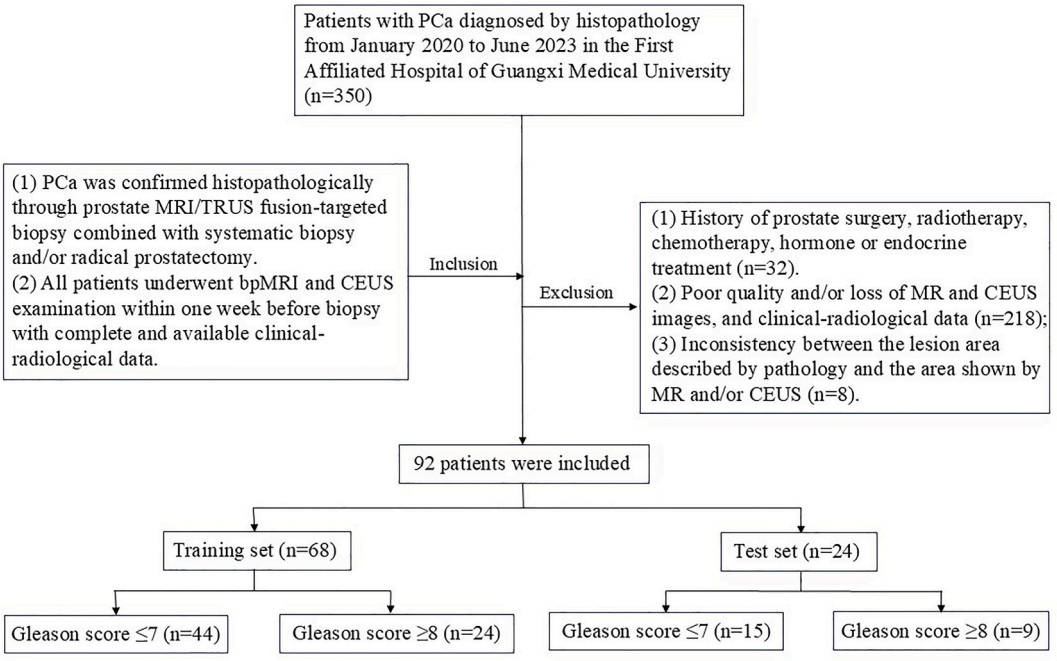

Fig. 1. Flowchart of the patient enrollment process.

subregions and the omics characteristics of CEUS to predict high-risk PCa [22,23].

The purpose of this study was to identify tumor habitat subregions with similar biological characteristics from bp-MRI, develop quantitative measurement methods for intratumoral heterogeneity through radiomics analysis, and combine clinical indicators and CEUS omics characteristics to predict the preoperative value of high-risk PCa.

2. Materials and Methods

2.1. Patients

This retrospective study was approved by the Ethics Committee and waived the need for informed consent (Approval Number: 2023-E202-01). We retrospectively collected patients with PCa confirmed by histopathology from January 2020 to June 2023. A total of 350 consecutive patients were analyzed in this study. The processes of the inclusion and exclusion of the study subjects are shown in Fig. 1. Finally, 92 patients were enrolled and randomly divided into the training set and the test set, with a ratio of 7:3. The patients were categorized into two groups based on pathological reports [24]: the intermediate-low-risk group (Gleason score $\leq$7) and the high-risk group (Gleason score $\geq$8).

2.2. MRI examination

Bp-MRI was performed using Siemens MAGNETOM Viro 3.0T MRI imager and Siemens MAGNETOM Prisma 3.0T MRI imager (Siemens, Munich, Germany). MR imaging protocols included T2WI/T2WI-FS and DWI imaging sequences. Detailed scanning protocols were shown in Supplement materials Table S1. The apparent diffusion coefficient (ADC) values were calculated from the mono-exponential signal attenuation model of the DWI images, and the ADC maps were reconstructed through automatic post-processing of

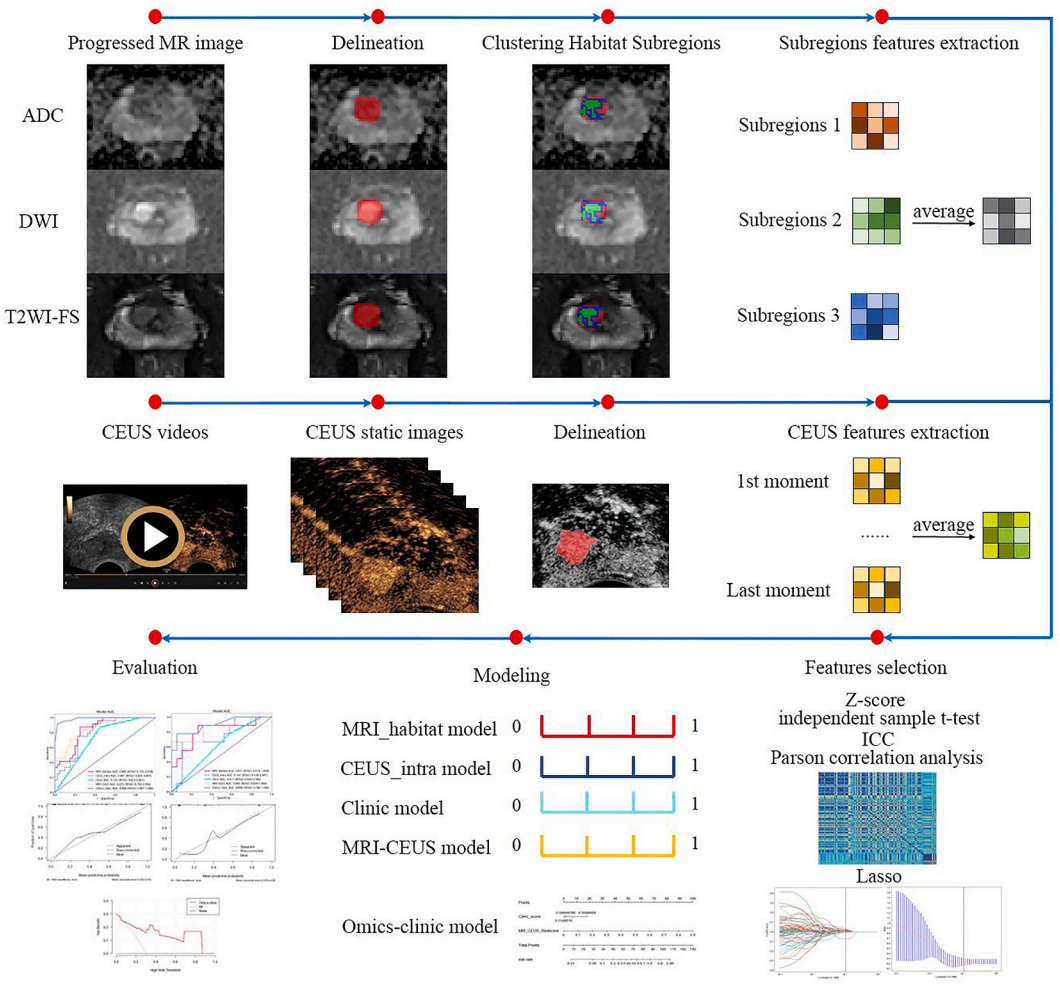

Fig. 2. Schematic of the workflow of the high-risk PCa prediction method used in this study.

the MR scanner. The bp-MRI imaging results of all subjects were interpreted by two experienced radiologists. When there were differences in the conclusions, a consensus was reached through discussion.

2.3. CEUS examination

CEUS examinations were performed using LOGIQ E9 ultrasound equipment (GE Healthcare, Milwaukee, WI, USA), transrectal probe IC5-9-D, with a frequency of 3–9 MHz. The CEUS examination was performed by a senior sonographer with 10 years of CEUS experience. During the examination, the patient was placed in the left lateral position with the legs flexed and the hands clasped around the knees. Conventional transrectal ultrasound (TRUS) was performed to observe the shape, size, and whether there were nodules or abnormal blood flow signals of the prostate. After real-time fusion of the MRI and ultrasound images, suspicious lesions of the prostate indicated by the MRI were located, and CEUS was performed on this plane. A 2.4 mL ultrasound contrast agent (SonoVue, Bracco Imaging, Milan, Italy) was rapidly injected through the median vein of the elbow, and 5 mL of physiological saline was used to quickly flush the tube. The contrast-enhanced appearance of the prostate was observed for 3 min. The data were recorded and stored in Digital Imaging and Communications in Medicine (DICOM) format.

2.4. Transrectal prostate biopsy and pathology

Bp-MRI data stored in DICOM format was uploaded in Volume Navigation (VNav, General Electric, USA), which is an image fusion software installed on the ultrasound equipment (LOGIQ E9, GE). In the navigation mode, ultrasound images and MRI images were manually adjusted by using the "surface-point" matching method. An 18 G automatic biopsy gun (CR Bard Inc., Tempe, AZ, USA) was used to perform MRI/TRUS fusion-targeted biopsy on suspicious lesions to get 1–3 cores, followed by systematic biopsy to get 12 cores. The pathology results and prostate cancer Gleason score were reported by experienced pathologists.

2.5. MRI processing and delineation

We used the affine registration and rigid registration methods of ITK-SNAP software (version 4.0) to simultaneously register the region of interest (ROI) of the same lesion on three sequence images: T2WI-FS, DWI (b = 1000 s/mm2), and ADC. To avoid the effect of uneven signal intensity in the MR images caused by magnetic field changes in the subsequent analysis, we used the N4 bias correction method to process all MR images [25]. To standardize the voxel spacing and minimize the differences in the radiomics features caused by different voxel sizes, all MR images were resampled to $1 \times 1 \times 1$ mm^3 due to the resolution difference.

A senior radiologist delineated the ROI along the lesion on the MR images layer by layer and then obtained the volume of interest (VOI) of the tumor. Due to the partial volume effect of the MRI [26], the radiologist carefully delineated the ROI slightly smaller than the boundary of the lesion during the delineation process while avoiding structures such as the urethra, ejaculatory duct, and seminal vesicle. If multiple lesions coexisted, the lesion with the highest Gleason score was selected for delineation. If the Gleason scores were the same, the lesion with the largest diameter was selected for delineation. The delineation results were confirmed by another senior radiologist. When differences were found, conclusions were reached through discussion. The delineation processes are shown in Fig. 2.

2.6. CEUS processing and delineation

The dynamic CEUS video was converted into static images, which were obtained every 5 s, starting from the infusion of the contrast agent. A total of 979 contrast static images were obtained. A senior sonographer delineated the ROI of the tumor based on the peak time of CEUS. The delineation results were confirmed by the other senior sonographer. When differences were found, conclusions were reached through discussion. The obtained ROI was matched with the other static images of the same patient at different time points. The delineation processes are shown in Fig. 2. The intraclass correlation coefficient (ICC) was calculated to evaluate the consistency between the radiomics features extracted from the ROI. The radiomics features with ICC $\geq$0.75 were considered to have good repeatability and stability and were retained for the subsequent feature selection procedure.

2.7. Spatial tumor habitats from the MRI

Habitat subregions were divided using a K-mean clustering algorithm based on the T2WI-FS, DWI, and ADC imaging sequences. The Euclidean distance between voxel intensities was used as a similarity metric to optimize the clustering process. K values (2, 3, 4, or 5) and the average Calinski-Harabasz (CH) scores for different k values were calculated to evaluate the clustering results (Supplement materials Fig. 1). We chose k = 3 as the optimal number of clusters with reference to the CH score, which means that three habitat subregions were generated. All processes of habitat analysis are illustrated in Fig. 2.

2.8. Features extraction

We extracted the radiomics features by PyRadiomics (version 3.0.1) package in Python (version 3.7) [27]. For the MRI, the radiomics features were extracted from each habitat subregion of each imaging sequence. A total of 949 features were extracted from a single habitat subregion of a single imaging sequence. At the individual level, the features of all habitat subregions of the same imaging sequence were averaged. Then, 2847 features were extracted from each habitat subregion from the three imaging sequences. For the

CEUS, the radiomics features of each patient were extracted from the ROIs of all the contrast moment images. Aside from the abovementioned features, shape and first-order features were also extracted, totally of 1561 features. For the same patient, the average of the features from all the contrast images was taken to represent this patient. We also combined the features derived from habitat subregions of the MRI and those from CEUS to construct omics–clinic prediction models.

2.9. Omics features selection and model construction

First, to achieve a zero mean and unit variance, all the radiomics features were normalized using Z-score. The features with $P < 0.05$ were retained for preliminary screening using the independent samples *t*-test. Thereafter, the correlation between the features was analyzed using the Pearson correlation coefficient. One out of two highly correlated features with a correlation coefficient >0.9 was randomly retained. Finally, the features with non-zero coefficients were filtered out, which were using the least absolute shrinkage and selection operator (LASSO) algorithm, and 10-fold cross-validation.

The filtered features were input into the multilayer perceptron (MLP) machine learning model. A 10-fold cross-validation was used in the training set to obtain the best parameters for the model. Radiomics prediction models, namely, MRI_habitat, CEUS_intra, and MRI-CEUS models, were developed based on the habitat features of bp-MRI, the omics features of CEUS, and a merge of features of the two, respectively. Predicted probabilities, called radscores, were then obtained.

2.10. Clinical-radiological indicators selection and model construction

The clinical indicators [age, body mass index (BMI), total prostate-specific antigen (T-PSA), free-PSA (F-PSA), F-PSA/T-PSA (F/T), prostate volume (PV), PSA density (PSAD), alkaline phosphatase (ALP), albumin (ALB), lymphocyte (LYM), neutrophil (NEU), mononuclear (MONO), neutrophil to lymphocyte count ratio (NLR)] and radiological indicators [PI-RADS v2.0 score, peak intensity (PI), time to peak (TTP), bone metastasis (BM)] were used as candidate variables. Univariate logistic regression analysis was used to initially screen out the variables. Multivariate logistic regression analysis was used to determine the independent risk factors. A clinical prediction model was constructed by inputting the independent risk factors into the logistic regression (LR) machine learning model to obtain the predicted probabilities called the clinic score.

3. Omics–clinic model construction

The clinic score and the radscore of the MRI-CEUS model were inputted into AdaBoost machine learning to construct an omics–clinic prediction model. A nomogram was plotted to visualize the omics–clinic prediction model [28]. The prediction performance among the omics–clinic model, clinic model and MRI-CEUS model was compared respectively.

Table 1
Clinical-radiological indicators of the patients in different sets.

Indicators	Total (n = 92)	Training set (n = 64)	Test set (n = 28)	p value
Age	67.8 ± 7.7	69.0 ± 7.4	64.9 ± 8.0	0.018
BMI	23.9 (21.7–25.9)	23.9 (21.5–25.5)	23.6 (22.0–27.1)	0.530
T-PSA	21.0 (11.2–78.5)	20.7 (10.6–71.0)	21.5 (12.8–92.5)	0.859
F-PSA	2.6 (1.3–8.6)	2.6 (1.2–7.4)	2.6 (1.3–9.4)	0.993
F/T	0.1 (0.1–0.2)	0.1 (0.1–0.2)	0.1 (0.1–0.2)	0.980
PV	40.2 (31.3–52.6)	29.8 (331.3–52.4)	42.5 (30.3–55.8)	0.757
PSAD	0.6 (0.3–1.9)	0.6 (0.3–1.6)	0.7 (0.3–2.3)	0.722
ALP	84.5 (69.0–104.8)	86.5 (70.0–104.0)	74.0 (67.0–104.8)	0.366
ALB	41.3 (38.5–42.9)	41.5 (38.1–42.9)	41.0 (38.9–43.0)	0.690
LYM	1.6 (1.3–2.0)	1.6 (1.3–2.1)	1.6 (1.4–1.9)	0.865
NEU	3.7 (3.1–4.6)	3.9 (3.2–4.7)	3.7 (3.0–4.4)	0.564
MONO	0.5 (0.4–0.7)	0.5 (0.4–0.7)	0.5 (0.4–0.6)	0.608
NLR	1.8 (0.2–2.7)	1.9 (0.2–2.6)	1.7 (0.9–3.0)	0.835
PI	21.3 ± 4.9	20.98 ± 5.14	21.89 ± 4.18	0.413
TTP	10.6 (8.3–13.8)	11.1 (8.3–14.0)	10.2 (7.8–13.7)	0.789
PI-RADS v2.0 score				0.715
2	2 (2.2 %)	2 (3.1 %)	0	
3	6 (6.5 %)	4 (6.3 %)	2 (7.1 %)	
4	27 (29.3)	19 (29.7 %)	8 (28.6 %)	
5	57 (62.0 %)	39 (60.9 %)	18 (64.3 %)	
BM				0.646
non-metastasis	66 (71.7 %)	45 (70.3 %)	21 (75.0 %)	
metastasis	26 (28.3 %)	19 (29.7 %)	7 (25.0 %)	

95 % confidence interval (95%CI), body mass index (BMI), total prostate-specific antigen (T-PSA), free prostate-specific antigen (F-PSA), F/T, prostate volume (PV), PSA density (PSAD), alkaline phosphatase (ALP), albumin (ALB), lymphocyte (LYM), neutrophil (NEU), mononuclear (MONO), neutrophil-to-lymphocyte count ratio (NLR), prostate imaging reporting and data system v2.0 score (PI-RADS v2.0 score), peak intensity (PI), time to peak (TTP), and bone metastasis (BM).

3.1. Model performance evaluation

To assess the performance of all prediction models, we plotted the receiver operating characteristic (ROC) curve and calculated the AUC, accuracy, precision, sensitivity, specificity, positive predictive value, negative predictive value, recall, and F1 score. The Hosmer–Lemeshow test was used to evaluate the concurrence among the anticipated results of the models and the histopathological results. The calibration curves were drawn to visualize the predictive accuracy of the models [29]. Decision curve analysis (DCA) was used to quantify the net benefit, which can assess the clinical practicability of the models across different threshold probabilities [30].

3.2. Statistical analysis

The Kolmogorov–Smirnov test was used to test the normality of data. The Student's t-test was used for continuous variables with a normal distribution, which was expressed as mean ± standard deviation. Abnormal distributed continuous variables were expressed as the median (interquartile range), which was using Mann Whitney *U* test. The categorical variables were expressed as frequencies or percentages, which was using chi-square test or Fisher's exact test.

The DeLong test was used to compare the differences in the AUC between different models. $P < 0.05$ was considered statistically significant. Data processing, model construction, statistical analysis, and model evaluation were conducted using Python (version 3.7), R software (version 4.2.2), and SPSS (version 27.0.1).

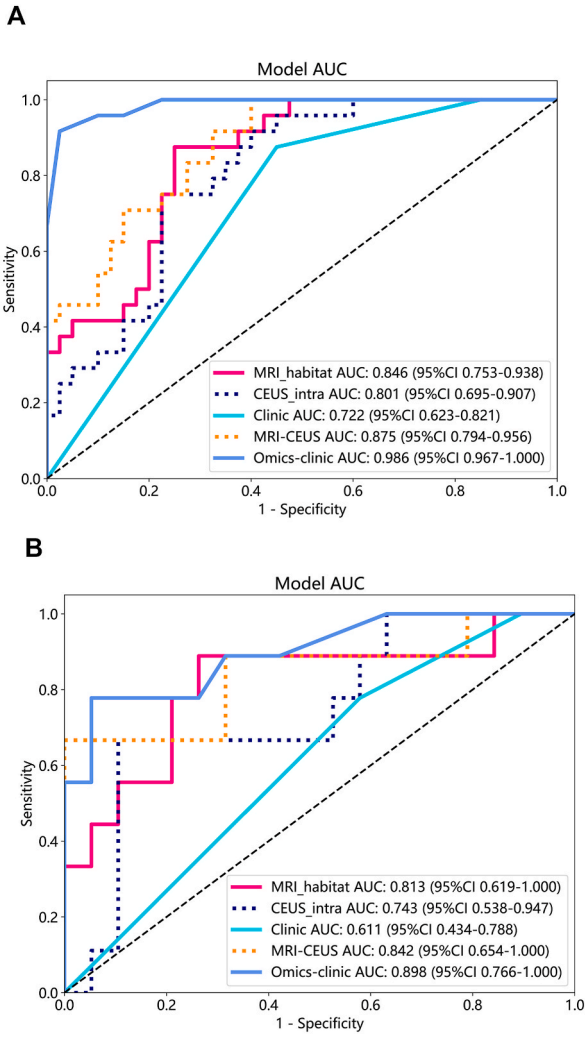

Fig. 3. ROC curves in the training set (A) and test set (B).

4. Results

4.1. Patient population

A total of 92 patients (mean age: 67.8 ± 7.7 years; range: 47–83 years) were included in the study. Among these patients, 59 had a Gleason score ≤7 (mean age: 66.8 ± 7.9 years; range: 47–82 years), and 33 had a Gleason score ≥8 (mean age: 69.4 ± 7.3 years; range 55–83 years). There were 64 patients in the training set and 28 patients in the test set. The clinical-radiological indicators of the patients in the training set and test set are presented in Table 1.

4.2. Performance of models

In distinguishing intermediate-low-risk PCa from high-risk PCa, the ROC curves are shown in Fig. 3. The results of the univariate and multivariate logistic regression analyses in the training set are presented in Table 2. The performance of the diagnosis of the models are shown in Table 3 and Supplement materials Fig. 2. The nomogram used to visualize the omics–clinic model is illustrated in Fig. 4. According to the calibration curves (Fig. 5), the deviation curves of the training and test sets of the omics–clinic model were close to the ideal curves. Fig. 6 shows the DCA of the omics–clinic model. The net benefit was measured by the y-axis. The DCA curve showed that implementing the omics–clinic models was more beneficial than either treating all patients (assuming all lesions were high risk) or providing no treatment (assuming all lesions were low risk). In addition, the threshold probability range of the omics–clinic model for obtaining the highest net benefit was the largest.

5. Discussion

In our study, we constructed multiple predictive models to identify high-risk PCa from intermediate-low-risk PCa. Through horizontal comparisons, the habitat subregion-based radiomics model was found to exhibit stronger predictive performance than the models relying on CEUS intratumoral radiomics features and clinical-radiological indicators. In addition, integrating the habitat subregion-based radiomics of the MRI with the intratumoral region-based radiomics of CEUS and clinical-radiological indicators facilitated further improvement in predictive ability.

Previous research focusing on prostate MRI has predominantly conducted radiomics analysis of the entire lesion. Jin et al. [31] developed an omics–clinic model to predict the occurrence of clinically significant PCa, with a mean AUC of 0.803. In contrast to previous studies, our study divided the entire tumor into distinct habitat subregions based on the similarities and differences in the prostate MRI voxel features and constructed a prediction model utilizing the radiomics features from those subregions. The AUCs of the MRI_habitat model in predicting the risk of PCa in the training set and test set were 0.846 and 0.813, respectively.

PCa is characterized by massive angiogenesis and infiltration, resulting in a complex vascular distribution, leading to different blood supply statuses in various regions of the tumor. Alterations in blood flow can drive changes in the surrounding microenvironment, such as hypoxia, acidosis, and necrosis [32]. Moreover, the progression of PCa is frequently accompanied by the infiltration of immune cells, which can secrete cytokines and chemokines that affect tumor growth [33]. Due to the presence of multiple factors,

Table 2
Results of the univariate and multivariate logistic regression analysis in the training set.

Indicators	Univariate logistic regression		Multivariate logistic regression	
	OR (95%CI)	p value	OR (95%CI)	p value
Age	1.042 (0.970–1.120)	0.262		
BMI	0.896 (0.744–1.078)	0.244		
T-PSA	1.007 (0.999–1.014)	0.078		
F-PSA	1.076 (1.019–1.137)	0.009	1.054 (0.978–1.136)	0.167
F/T	0.000 (0.000–0.338)	0.029	0.000 (0.000–3.630)	0.081
PV	1.008 (0.980–1.037)	0.575		
PSAD	1.257 (0.987–1.601)	0.064		
ALP	1.000 (0.998–1.001)	0.596		
ALB	0.885 (0.784–0.999)	0.048	1.014 (0.857–1.200)	0.872
LYM	0.643 (0.300–1.381)	0.258		
NEU	0.837 (0.524–1.337)	0.457		
MONO	0.479 (0.033–6.900)	0.589		
NLR	0.899 (0.648–1.246)	0.522		
PI	1.105 (0.987–1.237)	0.082		
TTP	0.989 (0.889–1.101)	0.845		
PI-RADS v2.0 score	6.876 (1.872–25.250)	0.004	4.365 (1.080–17.640)	0.039
BM	2.460 (0.819–7.389)	0.109		

95 % confidence interval (95%CI), body mass index (BMI), total prostate-specific antigen (T-PSA), free prostate-specific antigen (F-PSA), F/T, prostate volume (PV), PSA density (PSAD), alkaline phosphatase (ALP), albumin (ALB), lymphocyte (LYM), neutrophil (NEU), mononuclear (MONO), neutrophil-to-lymphocyte count ratio (NLR), prostate imaging reporting and data system v2.0 score (PI-RADS v2.0 score), peak intensity (PI), time to peak (TTP), and bone metastasis (BM).

Table 3
The performance comparison of different models.

Models	Set	AUC (95%CI)	ACC	SEN	SPE	PPV	NPV	PRE	Recall	F1 score
MRI_habitat	training	0.846 (0.753–0.938)	0.797	0.750	0.875	0.909	0.677	0.909	0.750	0.822
	test	0.813 (0.619–1.000)	0.786	0.737	0.889	0.933	0.615	0.933	0.737	0.824
CEUS_intra	training	0.801 (0.695–0.907)	0.766	0.775	0.750	0.838	0.667	0.838	0.775	0.805
	test	0.743 (0.538–0.947)	0.821	0.895	0.667	0.850	0.750	0.850	0.895	0.872
Clinic	training	0.722 (0.623–0.821)	0.672	0.550	0.875	0.880	0.538	0.880	0.550	0.677
	test	0.611 (0.434–0.788)	0.536	0.421	0.778	0.800	0.389	0.800	0.421	0.552
MRI-CEUS	training	0.875 (0.794–0.956)	0.750	0.600	1.000	1.000	0.600	1.000	0.600	0.750
	test	0.842 (0.654–1.000)	0.893	1.000	0.667	0.864	1.000	0.864	1.000	0.927
Omics-clinic	training	0.986 (0.967–1.000)	0.953	0.975	0.917	0.951	0.957	0.951	0.975	0.963
	test	0.898 (0.766–1.000)	0.893	0.947	0.778	0.900	0.875	0.900	0.947	0.923

Area under the curve (AUC), 95 % confidence interval (95%CI), accuracy (ACC), sensibility (SEN), specificity (SPE), positive predictive value (PPV), negative predictive value (NPV), precision (PRE).

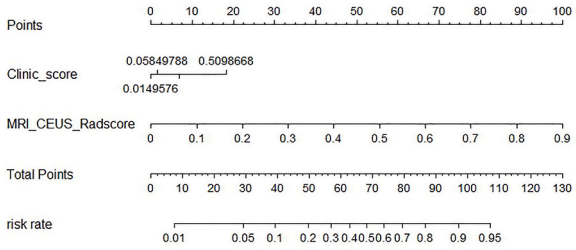

Fig. 4. A radiomics nomogram was developed using the clinic score and the MRI-CEUS radscore for the prediction of high-risk PCa in the training set.

the heterogeneous pattern of prostate cancer is often not uniformly distributed [18]. Habitat analysis can capture the aforementioned subtle changes in the tumor, combine the tumor cells with the microenvironment in which they proliferate, reflect the pathophysiological changes throughout tumor growth, and more appropriately characterize the spatial heterogeneity within the tumor. Our results suggest that narrowing the focus from the entire tumor region to the habitat subregions can provide more valuable information for the grading and prognostic analyses of PCa.

Previous studies have demonstrated the diagnostic value of CEUS in identifying benign and malignant prostate lesions [34,35]. In contrast to studies using quantitative measures of CEUS or using only the radiomics features from CEUS images at specific moments, we innovatively extracted and fused the radiomics features from CEUS images at multiple moments to assess the value of CEUS for predicting the risk of PCa. The AUCs of the CEUS_intra model in the training set and test set were 0.801 and 0.743, respectively.

To further evaluate the predictive value of the habitat subregions combined with CEUS, we incorporated the radiomics features of the habitat subregions of MRI and those of the intratumoral regions of CEUS to construct the MRI-CEUS model. The results in our study showed that the AUCs of the bpMRI-CEUS model were elevated compared with those of the individual models in the training and test sets. These results indicate that the radiomics features of the habitat subregions and CEUS have the potential to complement each other. Although both CEUS and DCE-MRI can provide information about tumor blood supply, DCE-MRI reflects signal intensity versus time rather than visualizing changes in the contrast concentration over time [14]. In this regard, CEUS has an advantage.

Xiang et al. [36] developed a clinic model to differentiate PCa with an AUC of 0.748. In this study, the AUC of the clinic model was 0.722. There is a risk of overdiagnosis and overtreatment of PCa by relying only on clinical indicators for diagnosis and assessment [37,38]. Therefore, we integrated the radiomics features of the habitat subregions of the MRI, the intratumoral regions of CEUS and the clinical-radiological indicators to construct an omics–clinic model. The AUCs of the omics–clinic model were 0.986 and 0.898 in the training set and test set, respectively, showing that this model may be a powerful tool to assist clinicians in assessing the risk of PCa.

Our study has some limitations. First, this retrospective study was a single center. Therefore, the sample population was small, with potential population selectivity bias. In the future, we need to work with other institutions to incorporate more samples and conduct multicenter studies. Second, the habitat subregions generated by clustering were not confirmed by rigorous pathology. Third, the delineation of habitat subregions using voxels from multiple imaging sequences requires the spatial registration of all imaging sequences. However, there may be resolution differences and distortions between the different imaging sequences, which may affect the results of the registration.

6. Conclusion

The habitat radiomics analysis strategy we developed in this study based on bp-MRI may be a valuable tool for identifying high-risk

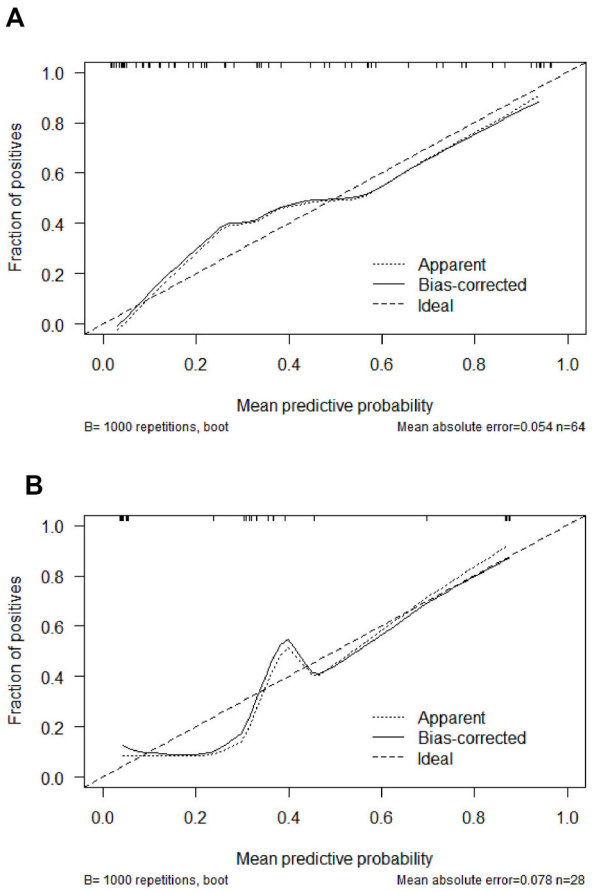

Fig. 5. Calibration curves of the MRI-CEUS model in the training set (A) and test set (B).

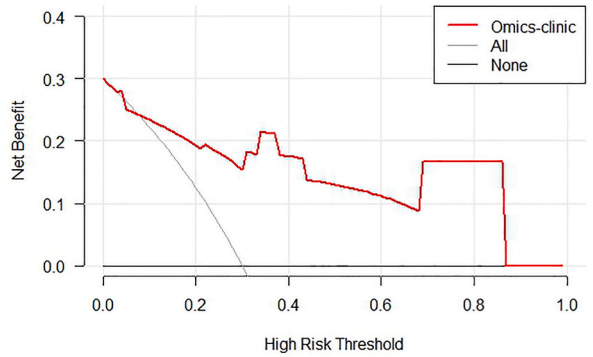

Fig. 6. Decision curve analysis of the MRI-CEUS model in the test set.

PCa. The model integrating the radiomics features of the habitat subregions of the MRI and the intratumoral regions of CEUS and the clinical-radiological indicators showed a favorable identifying capability.

Funding

This work was supported by “National Natural Science Foundation of China Youth Science Fund Project” (Grant number: 82001827) and “Guangxi Natural Science Foundation of General Project” (Grant number: 2024GXNSFAA010249).

Data availability statement

The data that support the findings of this study are available from the corresponding author upon reasonable request.

CRediT authorship contribution statement

Fangyi Huang: Writing – original draft. **Qun Huang:** Data curation. **Xinhong Liao:** Investigation. **Yong Gao:** Writing – review & editing, Funding acquisition.

Declaration of competing interest

The authors declare that they have no known competing financial interests or personal relationships that could have appeared to influence the work reported in this paper.

Appendix A. Supplementary data

Supplementary data to this article can be found online at https://doi.org/10.1016/j.heliyon.2024.e37955.

References

[1] H. Sung, J. Ferlay, R.L. Siegel, M. Laversanne, I. Soerjomataram, A. Jemal, et al., Global cancer statistics 2020: GLOBOCAN estimates of incidence and mortality worldwide for 36 cancers in 185 countries, CA Cancer J Clin 71 (3) (2021) 209–249.
[2] C. Xia, X. Dong, H. Li, M. Cao, D. Sun, S. He, et al., Cancer statistics in China and United States, 2022: profiles, trends, and determinants, Chin Med J (Engl). 135 (5) (2022) 584–590.
[3] K.A. Moses, P.C. Sprenkle, C. Bahler, G. Box, S.V. Carlsson, W.J. Catalona, et al., NCCN Guidelines® insights: prostate cancer early detection, version 1.2023, J Natl Compr Canc Netw 21 (3) (2023) 236–246.
[4] N. Mottet, R.C.N. van den Bergh, E. Briers, T. Van den Broeck, M.G. Cumberbatch, M. De Santis, et al., EAU-EANM-ESTRO-ESUR-SIOG guidelines on prostate cancer-2020 update. Part 1: screening, diagnosis, and local treatment with curative intent, Eur. Urol. 79 (2) (2021) 243–262.
[5] C.J. Das, A. Netaji, A. Razik, S. Verma, MRI-targeted prostate biopsy: what radiologists should know, Korean J. Radiol. 21 (9) (2020) 1087–1094.
[6] J.J. Park, C.K. Kim, Paradigm shift in prostate cancer diagnosis: pre-biopsy prostate magnetic resonance imaging and targeted biopsy, Korean J. Radiol. 23 (6) (2022) 625–637.
[7] Y. Yamada, T. Shiraishi, A. Ueno, T. Ueda, A. Fujihara, Y. Naitoh, et al., Magnetic resonance imaging-guided targeted prostate biopsy: comparison between computer-software-based fusion versus cognitive fusion technique in biopsy-naïve patients, Int. J. Urol. 27 (1) (2020) 67–71.
[8] M. Hung, A.E. Ross, E.V. Li, C.P. Pavlovich, S.A. Fletcher, S. Gereta, et al., Prostate cancer detection rate of transperineal prostate biopsy: cognitive vs software fusion, A multicenter analysis, Urology 186 (2024) 91–97.
[9] U.G. Falagario, F. Pellegrino, A. Fanelli, F. Guzzi, R. Bartoletti, H. Cash, et al., Prostate cancer detection and complications of MRI-targeted prostate biopsy using cognitive registration, software-assisted image fusion or in-bore guidance: a systematic review and meta-analysis of comparative studies, Prostate Cancer Prostatic Dis. (2024).
[10] M. Gerlinger, A.J. Rowan, S. Horswell, M. Math, J. Larkin, D. Endesfelder, et al., Intratumor heterogeneity and branched evolution revealed by multiregion sequencing, N. Engl. J. Med. 366 (10) (2012) 883–892.
[11] T. Chen, Z. Zhang, S. Tan, Y. Zhang, C. Wei, S. Wang, et al., MRI based radiomics compared with the PI-rads V2.1 in the prediction of clinically significant prostate cancer: biparametric vs multiparametric MRI, Front. Oncol. 11 (2021) 792456.
[12] P. De Visschere, N. Lumen, P. Ost, K. Decaestecker, E. Pattyn, G. Villeirs, Dynamic contrast-enhanced imaging has limited added value over T2-weighted imaging and diffusion-weighted imaging when using PI-RADSv2 for diagnosis of clinically significant prostate cancer in patients with elevated PSA, Clin. Radiol. 72 (1) (2017) 23–32.
[13] C.F. Wan, X.S. Liu, L. Wang, J. Zhang, J.S. Lu, F.H. Li, Quantitative contrast-enhanced ultrasound evaluation of pathological complete response in patients with locally advanced breast cancer receiving neoadjuvant chemotherapy, Eur. J. Radiol. (2018) 1872–7727 (Electronic)).
[14] R. Stoyanova, F. Chinea, D. Kwon, I.M. Reis, Y. Tschudi, N.A. Parra, et al., An automated multiparametric MRI quantitative imaging prostate habitat risk scoring system for defining external beam radiation therapy boost volumes, Int. J. Radiat. Oncol. Biol. Phys. 102 (4) (2018) 821–829.
[15] X. Zhu, L. Shao, Z. Liu, Z. Liu, J. He, J. Liu, et al., MRI-derived radiomics models for diagnosis, aggressiveness, and prognosis evaluation in prostate cancer, J. Zhejiang Univ. - Sci. B 24 (8) (2023) 663–681.
[16] M.R. Tomaszewski, R.J. Gillies, The biological meaning of radiomic features, Radiology 298 (3) (2021) 505–516.
[17] R. Castaldo, C. Cavaliere, A. Soricelli, M. Salvatore, L. Pecchia, M. Franzese, Radiomic and genomic machine learning method performance for prostate cancer diagnosis: systematic literature review, J. Med. Internet Res. 23 (4) (2021) e22394.
[18] R.A. Gatenby, O. Grove, R.J. Gillies, Quantitative imaging in cancer evolution and ecology, Radiology 269 (1) (2013) 8–15.
[19] M. Kim, J.E. Park, S.K. Yoon, N. Kim, Y.H. Kim, J.H. Kim, et al., Vessel size and perfusion-derived vascular habitat refines prediction of treatment failure to bevacizumab in recurrent glioblastomas: validation in a prospective cohort, Eur. Radiol. 33 (6) (2023) 4475–4485.
[20] A.S. Kazerouni, D.A. Hormuth 2nd, T. Davis, M.J. Bloom, S. Mounho, G. Rahman, et al., Quantifying tumor heterogeneity via MRI habitats to characterize microenvironmental alterations in HER2+ breast cancer, Cancers 14 (7) (2022).
[21] E. Sala, E. Mema, Y. Himoto, H. Veeraraghavan, J.D. Brenton, A. Snyder, et al., Unravelling tumour heterogeneity using next-generation imaging: radiomics, radiogenomics, and habitat imaging, Clin. Radiol. 72 (1) (2017) 3–10.
[22] N.A. Parra, H. Lu, J. Choi, K. Gage, J. Pow-Sang, R.J. Gillies, et al., Habitats in DCE-MRI to predict clinically significant prostate cancers, Tomography 5 (1) (2019) 68–76.
[23] Y. Tschudi, A. Pollack, S. Punnen, J.C. Ford, Y.C. Chang, N. Soodana-Prakash, et al., Automatic detection of prostate tumor habitats using diffusion MRI, Sci. Rep. 8 (1) (2018) 16801.
[24] A. Gurwin, K. Kowalczyk, K. Knecht-Gurwin, P. Stelmach, Ł. Nowak, W. Krajewski, et al., Alternatives for MRI in prostate cancer diagnostics-review of current ultrasound-based techniques, Cancers 14 (8) (2022).
[25] N.J. Tustison, B.B. Avants, P.A. Cook, Y. Zheng, A. Egan, P.A. Yushkevich, et al., N4ITK: improved N3 bias correction, IEEE Trans Med Imaging 29 (6) (2010) 1310–1320.

[26] M. Bernier, M. Chamberland, J.C. Houde, M. Descoteaux, K. Whittingstall, Using fMRI non-local means denoising to uncover activation in sub-cortical structures at 1.5 T for guided HARDI tractography, Front. Hum. Neurosci. 8 (2014) 715.
[27] J.J.M. van Griethuysen, A. Fedorov, C. Parmar, A. Hosny, N. Aucoin, V. Narayan, et al., Computational radiomics system to decode the radiographic phenotype, Cancer Res. 77 (21) (2017) e104–e107.
[28] Y. Gao, Y. Luo, C. Zhao, M. Xiao, L. Ma, W. Li, et al., Nomogram based on radiomics analysis of primary breast cancer ultrasound images: prediction of axillary lymph node tumor burden in patients, Eur. Radiol. 31 (2) (2020) 928–937.
[29] A.A. Kramer, J.E. Zimmerman, Assessing the calibration of mortality benchmarks in critical care: the Hosmer-Lemeshow test revisited, Crit. Care Med. 35 (9) (2007) 2052–2056.
[30] A.J. Vickers, A.M. Cronin, E.B. Elkin, M. Gonen, Extensions to decision curve analysis, a novel method for evaluating diagnostic tests, prediction models and molecular markers, BMC Med Inform Decis Mak 8 (2008) 53.
[31] P. Jin, J. Shen, L. Yang, J. Zhang, A. Shen, J. Bao, et al., Machine learning-based radiomics model to predict benign and malignant PI-RADS v2.1 category 3 lesions: a retrospective multi-center study, BMC Med Imaging 23 (1) (2023) 47.
[32] M. De Palma, D. Biziato, T.V. Petrova, Microenvironmental regulation of tumour angiogenesis, Nat. Rev. Cancer 17 (8) (2017) 457–474.
[33] A. Rani, P. Dasgupta, J.J. Murphy, Prostate cancer: the role of inflammation and chemokines, Am. J. Pathol. 189 (11) (2019) 2119–2137.
[34] Y. Sun, J. Fang, Y. Shi, H. Li, J. Wang, J. Xu, et al., Machine learning based on radiomics features combing B-mode transrectal ultrasound and contrast-enhanced ultrasound to improve peripheral zone prostate cancer detection, Abdom Radiol (NY) (2023).
[35] R.R. Wildeboer, C.K. Mannaerts, R.J.G. van Sloun, L. Budäus, D. Tilki, H. Wijkstra, et al., Automated multiparametric localization of prostate cancer based on B-mode, shear-wave elastography, and contrast-enhanced ultrasound radiomics, Eur. Radiol. 30 (2) (2020) 806–815.
[36] L. Xiang, S. Ma, Y. Xu, L. Jiang, H. Guo, H. Liu, et al., Patient-related characteristics predict prostate cancers in men with PI-RADS 4-5 to further optimize the diagnostic performance of MRI, Abdom Radiol (NY) (2023).
[37] O. Bergengren, K.R. Pekala, K. Matsoukas, J. Fainberg, S.F. Mungovan, O. Bratt, et al., 2022 update on prostate cancer epidemiology and risk factors-A systematic review, Eur. Urol. 84 (2) (2023) 191–206.
[38] K. Zhang, C.H. Bangma, M.J. Roobol, Prostate cancer screening in europe and asia, Asian J Urol 4 (2) (2017) 86–95.